J MATER SCI **41** (2006) 2559–2565

Comparison of the number densities of nanosized Cu-rich precipitates in ferritic alloys measured using EELS and EDX mapping, HREM and 3DAP

S. LOZANO-PEREZ, G. SHA, J. M. TITCHMARSH, M. L. JENKINS
Department of Materials, University of Oxford, Parks Rd., Oxford, OX1 3PH, UK

S. HIROSAWA
Ceramics Science, Tokyo Institute of Technology, O-okayama, Meguro-ku, Tokyo, 152–8552, Japan

A. CEREZO, G. D. W. SMITH
Department of Materials, University of Oxford, Parks Rd., Oxford, OX1 3PH, UK

In this paper we compare various microscopy methods which are used to characterize Cu-rich precipitates in pressure-vessel steels. EELS and EDX mapping is found to reveal Cu-rich precipitates of sizes greater than about 1–2 nm, both those with the bcc structure, which are coherent with the ferrite matrix, and incoherent transformed precipitates. This allows a direct comparison with results from 3DAP, which so far has been the only way to image such ultra-fine Cu-rich clusters. In HREM images only incoherent precipitates which have transformed to a twinned 9R structure are seen. A comparison is made of precipitate number densities and sizes as measured by EELS and EDX mapping, 3DAP and HREM.

1. Introduction

Fe–C–Ni–Mn–Si alloys such as ASME A508 and A533 have been used as reactor pressure-vessel (RPV) steels in commercial nuclear plants. However, the thermal exposure and neutron irradiation during operation gradually lead to the hardening and embrittlement of the alloys [1], at worst, forcing plant closure before the initially designed operation lifetime. This degradation in mechanical properties is known to be caused by the formation of nanoscale Cu-rich clusters [2]. Most of the thermal or radiation-induced precipitates are beyond or at the resolution limit of conventional transmission electron microscope (TEM) techniques such as diffraction contrast imaging, high-resolution microscopy or energy dispersive X-ray (EDX) mapping [3–7]. Electron energy loss (EELS) mapping, as well as other techniques not based on electron microscopy, such as small angle neutron scattering (SANS), atom probe microscopy and positron annihilation spectroscopy have however proven useful for quantifying the sizes and number densities of these precipitates [8–12]. In this paper we compare the performance of the TEM-based techniques with atom probe microscopy and consider their relative advantages and disadvantages.

2. Experimental procedures

2.1. Materials

The composition of the Fe–C–Ni–Mn–Si alloy chosen for this research is listed in Table I.

The alloy was prepared as a submerged arc weld, having a wide tapered "V" shape of thickness ∼150 mm and length 200–300 mm. The weld was annealed at 1193 ± 20 K for 21.6 ks and then quenched into water. Temper and stress relief treatments were carried out at 873 ± 15 K for 151.2 ks and at 923 ± 15 K for 21.6 ks, which was followed by slow in-furnace cooling at a rate $< 1.4 \times 10^{-2}$ K/s. The bulk sample was then sectioned into small blocks of size $15 \times 10 \times 10$ mm^3 which were sealed in quartz tubes to avoid oxidation. They were then aged at 638 or 678 K for 100, 1000, 3000 or 10000 h, and quenched in water.

After ageing, samples were made for both electron microscopy and atom probe analysis. For TEM, sheets were

0022-2461 © *2006 Springer Science + Business Media, Inc.*
DOI: 10.1007/s10853-006-7768-0

TABLE I Alloy composition in at%

C	Ni	Mn	Si	Cu	Mo	Cr	P	S	Fe
0.19	1.66	1.38	0.75	0.44	0.24	0.05	0.02	0.02	Bal

cut and thinned to 100 μm from which 3-mm discs were punched and electropolished in a Struers Tenupol 5 using a solution of 5% perchloric acid in methanol at 213 K. The specimens for atom probe analysis (using a three-dimensional atom probe, or 3DAP) were prepared using a two-stage electropolishing process, an initial polish in a solution of 25% perchloric acid and 75% acetic acid at 12 V followed by a second fine polish in a mixture of 2% perchloric acid and 98% 2-butoxyethanol at 15 V. Only two samples were chosen for TEM analysis. Sample A was treated at 678 K for 10000 h and sample B was treated at 638 K for 10000 h. These were the samples which were considered most likely to contain precipitates which could be resolved in the electron microscope.

2.2. TEM

A JEOL 3000F field-emission gun TEM (FEGTEM) was used for both energy-filtered and high-resolution imaging. This microscope is equipped with a Gatan energy-filter (GIF) which is controlled by Digital Micrograph v 3.1.1. The microscope was operated at 300 kV. More details about the operating conditions, including the optimisation of the signal-to-noise ratio (SNR) and the spatial resolution, can be found in [13].

A VG HB501 FEG-STEM equipped with an Oxford Instruments ultra-thin window energy-dispersive detector operated under Inca software was used for the EDX mapping. A probe size of 2 nm with a current of 0.5 nA was used in all the experiments.

2.3. 3D Atom Probe

3DAP analysis was performed using an energy-compensated optical position-sensitive atom probe (ECO-PoSAP) under ultra-high vacuum conditions i.e. $< 10^{-10}$ mbar. Details of the instrument can be found in [14, 15]. The tip temperature and pulse fraction were set to 60 K and 20%, as previously optimised for this alloy system [16]. Commercial 3DAP data analysis software (Oxford nanoScience) was used to generate atom maps and to determine the number density and composition of the precipitates present in the analysed volume.

3. Experimental results

3.1. 3DAP

Fig. 1 illustrates the Cu atom distributions from 3DAP analysis of samples aged at 638 K for different ageing times. From an initially homogeneous distribution, the first signs of Cu-rich clusters are just visible after 100 h.

TABLE II Measurements from 3D-AP of precipitate mean diameters and number densities for samples A and B

Samples	Heat treatment	N (10^{22}/m^3)	d_m (nm)
A	678 K 10000 h	3.0; ± 1.0	4.5 ± 0.6
B	638 K 10000 h	20.0 ± 2.0	3.8 ± 0.4

3DAP measurements results for the number density of copper-rich precipitates and their mean diameter d_m in samples A and B are shown in Table II

The small volume of each 3DAP analysis (typically $20 \times 20 \times 80$ nm^3) may result in high statistical errors when the cluster number density is low and few precipitates are detected within the volume analysed. The statistics can be improved significantly by carrying out multiple 3DAP analyses. The data above are based on three 3DAP runs for each ageing condition.

The composition of the Cu-rich precipitates could also be analysed in the 3DAP. Precipitates were identified in the data using the maximum separation method [10, 12], where all solute atoms closer than 0.4 nm were taken to belong to the same cluster. Only clusters determined to contain more than 50 solute atoms were treated as Cu-rich precipitates for the purpose of number density or composition calculations. Other atoms lying within 0.3 nm of any solute atom within a cluster are considered to be part of the cluster. However cluster atoms within 0.3 nm of the periphery of the precipitate are ignored for the purpose of calculating composition, to avoid a contribution from the matrix. Copper-rich clusters in our specimens contain several elements other than Cu, in particular Ni and Mn, which are not homogeneously distributed throughout the precipitate but are concentrated more in an outer shell. The cluster compositions which are obtained by the method described above then depend on which elements are taken as the solute atoms. If Cu, Ni and Mn are chosen as the solute atoms, the average composition for the precipitates in sample B was measured to be 20% Cu, 16% Ni, 14% Mn, 2% Si and 48% Fe. If only Cu atoms are considered as the solute, the average composition was found to be 43% Cu, 10% Ni, 8% Mn, 2% Si and 37% Fe. These differences may be understood as follows. In the former case the Ni and Mn atoms in the outer shell are incorporated into the precipitate, and so the composition obtained is an average over both the precipitate core and the outer shell. In the second case, the outer shell of Ni and Mn is not considered as part of the precipitate, and the composition measured is then representative of the precipitate core only. This description of the data analysis procedure has been provided so that the results can be compared with measurements from other techniques. The first definition is more relevant in the present work.

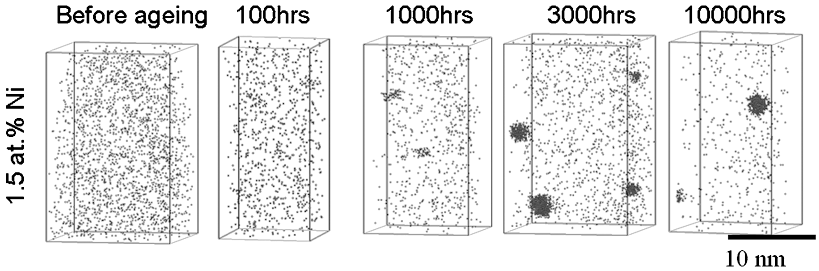

Figure 1 Cu atom distributions in samples aged at 638 K for different times.

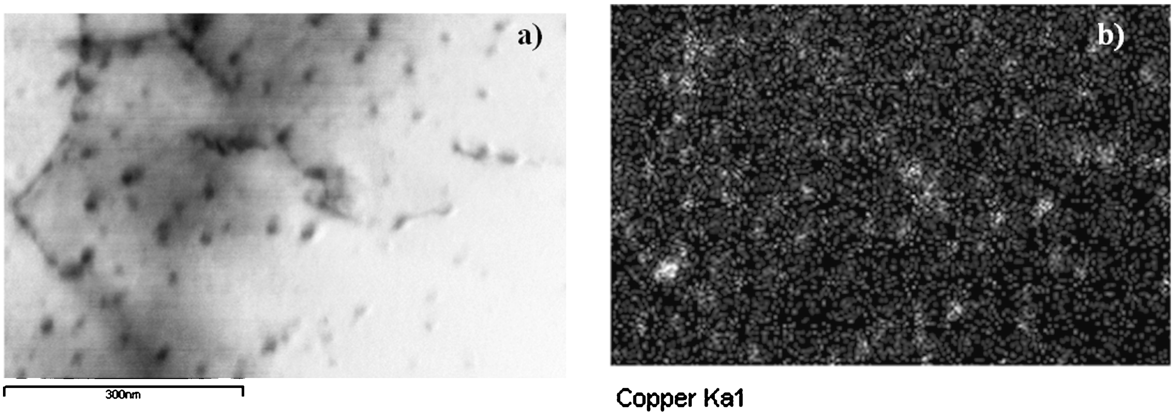

Figure 2 (a) STEM BF micrograph showing a region containing precipitates in Sample A, (b) EDX Cu K_α elemental map.

3.2. EDX mapping

256 × 224 pixel EDX maps were acquired in the VG STEM with a dwell time of 50 ms per pixel. The Cu maps revealed precipitates in both samples. Surprisingly, sample A was found to contain a moderate number density ($0.31 \pm 0.03 \times 10^{22}/\text{m}^3$) of comparatively large precipitates (>7 nm), with an average diameter of 12 ± 1 nm, which were not detected with the 3DAP. It was possible to see in high-magnification STEM bright-field images that another population of precipitates with smaller diameters was present, but many of these did not appear in EDX maps or appeared only very weakly. Spot analyses did however confirm that these small precipitates contained copper. In Fig. 2a, a region of sample A containing many incoherent precipitates is shown in a STEM bright-field image. It can be seen that many of the precipitates are associated with dislocations. In Fig. 2b, a Cu EDX elemental map shows that the positions of all the precipitates in Fig. 2a match with Cu-rich regions. Precipitate sizes were measured using line profiles on the elemental Cu maps. The results are shown in Table III, and were determined only from EDX maps, not from STEM images. In sample B a poor SNR led to large errors in the measurement of precipitate diameters, and the same is true of smaller precipitates in sample A. The errors shown in this and subsequent tables have been calculated as the standard deviation of the data (σ).

TABLE III Measurements from EDX maps of precipitate mean diameters and number densities for samples A and B

Sample	Heat treatment	N ($10^{22}/\text{m}^3$)	d_m (nm)
A	678 K 10000 h	4.1 ± 0.4	7.2 ± 0.8
B	638 K 10000 h	1.9 ± 0.8	3.5 ± 1.4

3.3. EELS mapping

Samples A and B were characterized using energy-filtered TEM (or EELS) imaging. Precipitates could be imaged using either the Cu or Fe L-edges. For quantitative analysis of the Cu-rich precipitates the Fe L_{23} edge was chosen. The reason for this is that the inelastic cross section of Fe is about 10 times larger than that of Cu. In other words, a certain volume of Fe produces an ionization edge with 10 times as many counts as the same volume of Cu, so it is easier to see the "lack" of Fe than the "increase" in Cu.

A series of 39 images with energy losses ranging from 650 to 1040 eV in steps of 10 eV and an energy-slit width of 10 eV were acquired (Fig. 3a). Then, a multi-window technique was used to fit the background and to form a background-subtracted post-edge image which can be used as an elemental Fe map (Fig. 3b). The elemental map using the Cu signal (930–1030 eV) generated in the same way confirmed that the Fe-depleted regions are Cu-rich (Fig. 3c).

Many different areas were analysed using this technique in order to determine the number densities and average

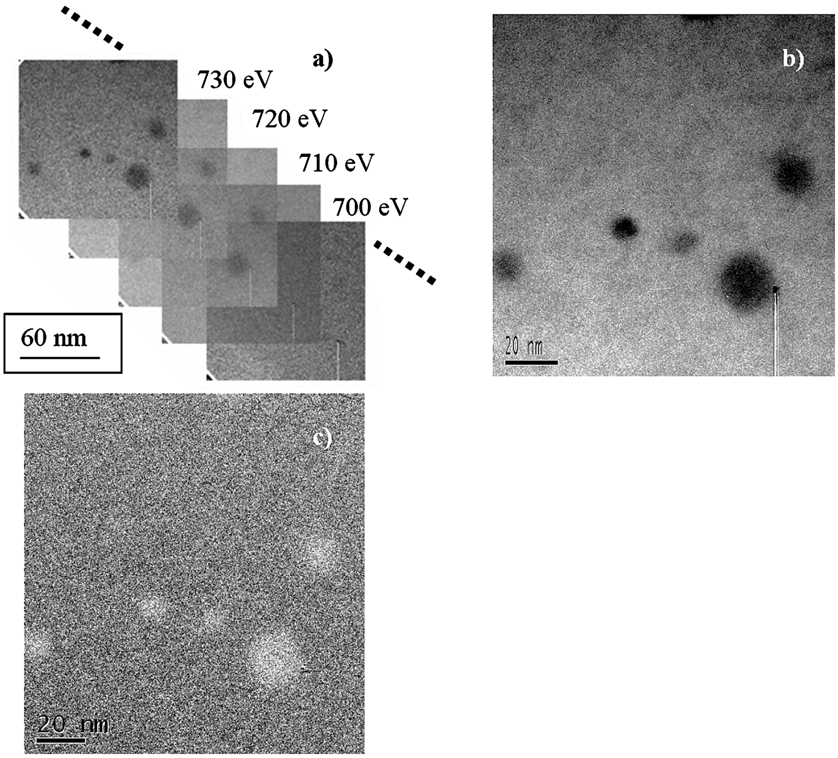

Figure 3 (a) energy-filtered (EF) series of images in sample A, sorted in energies, drift corrected and arranged as a 3D object (*x*, *y*, energy); (b) Fe map from sample A composed from 10 EF images (710–810 eV) using a 10 eV slit; (c) Cu map from sample A composed from 10 EF images (930–1030 eV) using a 10 eV slit.

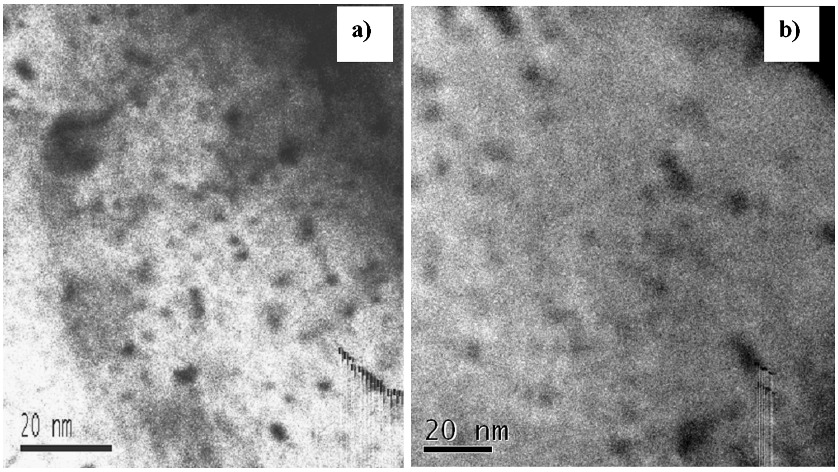

Figure 4 (a) Fe map from sample A calculated from 10 EF images (710–810 eV) using a 10 eV slit; (b) Fe map obtained in a similar way from sample B.

sizes of Cu-rich precipitates. In Fig. 4 an iron elemental map formed in the same way as in Fig. 3b is shown. The analysed area is thinner than in Fig. 3 and contains only one large precipitate and many small ones. A similar region was chosen for Sample B and is shown in Fig. 4b. The diameter of the particles was measured by fitting the data from a line profile across the particle on the Fe elemental map to the expected depletion on the signal due to the presence of a non-Fe spherical particle in the matrix. Details of this fitting technique can be found in reference [17]. Results for N and d_m are shown in Table IV. Histograms of size distributions are shown in Fig. 5.

TABLE IV Measurements from EELS maps of precipitate average diameters and number densities for samples A and B

Sample	Heat treatment	N $(\cdot 10^{22}/\mathrm{m}^3)$	d_m (nm)
A	678 K 10000 h	5.3 ± 0.9	6.0 ± 1.0
B	638 K 10000 h	6.1 ± 0.6	4.2 ± 0.3

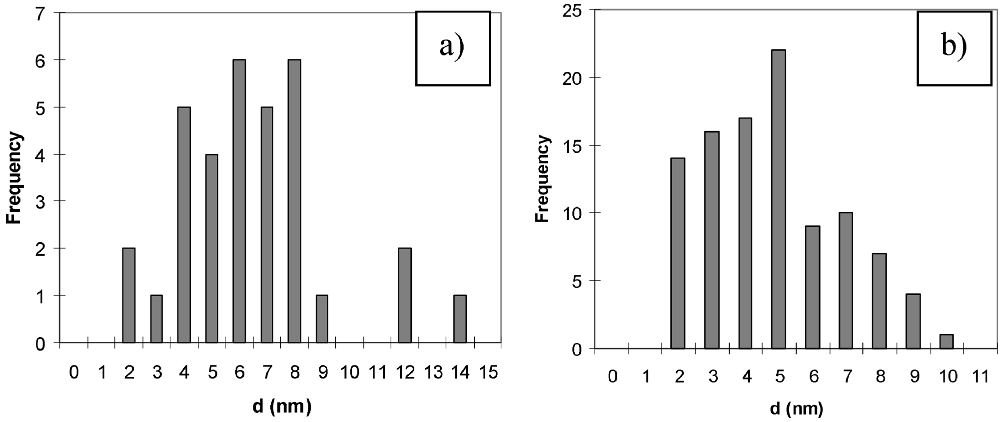

Figure 5 Histograms showing the precipitate size distributions (a) for sample A and (b) for sample B, obtained by EFTEM.

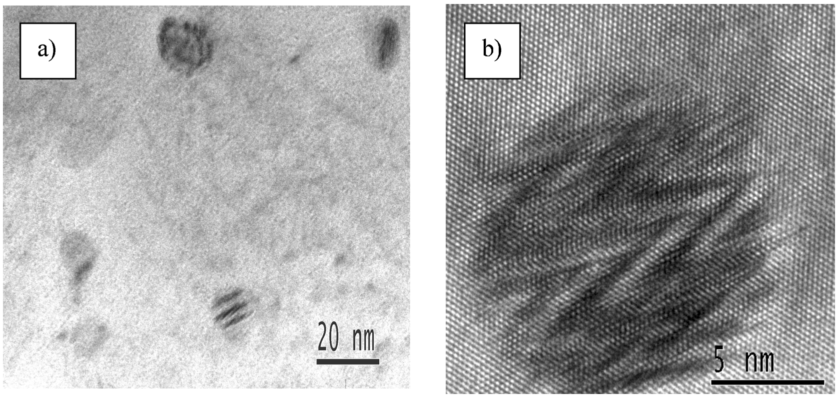

Figure 6 High-resolution TEM images of Cu-rich precipitates in alloy A.

3.4. HREM

All high-resolution images were acquired along the $<111>_{Fe}$ direction, at or near Scherzer focus. This direction is the optimum foil orientation for imaging the characteristic herring-bone fringe pattern within the multiply twinned precipitates [4]. The objective aperture was chosen to include the six $\{110\}_{Fe}$ reflections. Examples of the images acquired are shown in Figs 6a and b. The herring-bone pattern can be seen in Fig. 6b.

It was found that the thickness of the region examined had a major effect on the minimum diameter of the precipitates which could be observed. In thicker regions ($t \geq 40$ nm) precipitates smaller than ∼6 nm in diameter were not seen. In very thin regions ($t \leq$ 20 nm), precipitates as small as 3.5 nm were found.

Bright-field kinematical images revealed many smaller features, which should not be taken as Cu-rich precipitates without further confirmation (Fig. 7). Some other features could include carbides, making this technique unreliable if not used in conjunction with microanalysis in the TEM (EDX or EELS) or microdiffraction. In Tables V and VI, measurements of number densities and mean diameters made from high-resolution and bright-field images are shown.

TABLE V Measurements of average diameters and number densities of Cu-rich precipitates for samples A and B made from HREM images

Sample	Heat treatment	N $(\cdot 10^{22}/\text{m}^3)$	d_m (nm)
A	678 K 10000 h	3 ± 1	6 ± 2
B	638 K 10000 h	6 ± 3	3.7 ± 1.5

TABLE VI Measurements of average diameters and number densities of "small features" for samples A and B made from BF kinematical images

Sample	Heat treatment	N $(\cdot 10^{22}/\text{m}^3)$	d_m (nm)
A	678 K 10000 h	10.5 ± 0.8	4.2 ± 0.3
B	638 K 10000 h	9.2 ± 1.1	3.0 ± 0.4

4. Discussion

Some consistency is found between the results of the various techniques for both sizes and number densities, although there are also clear discrepancies. Only the 3DAP was able to find the smallest precipitates, resulting in a larger measured number density for sample B than any of the other methods. However this technique missed altogether the population of larger precipitates present in sample A which were seen by all the TEM techniques. The method suffers from poor statistics vis-à-vis the best

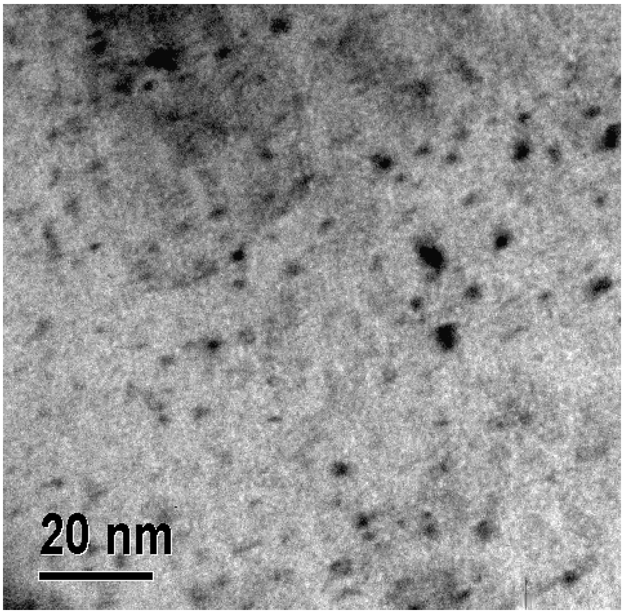

Figure 7 Bright-field kinematical image showing possible Cu-rich precipitates in sample A.

of the TEM techniques, EELS mapping. Poor statistics in the 3DAP is just a sampling problem, due to the small volume of the regions analysed, and can be improved by examining more specimens, which is very time-consuming, or by advances in the technique to allow larger volumes to be sampled. 3DAP provided very valuable information on the overall composition of the precipitates, which could not be measured easily with the other techniques (although we have recently developed a technique for measuring the iron content of precipitates from EELS maps, see [17]).

EDX was the less useful of the two TEM mapping techniques, with a more limited spatial resolution and a poorer SNR than EELS mapping. In sample B, EDX mapping picked up only the largest precipitates, and so the measured number density is much smaller than that found by the other methods. The VG STEM microscope was however capable of imaging precipitates with sizes down to 3 nm which gave EDX spectra enriched in Cu with respect to the matrix, but the relatively short dwell times prevented these precipitates from appearing in the Cu maps. Longer dwell times would have been unrealistic, as the spatial drift of the stage would have blurred the Cu signal. HREM was not very useful when the sample was thicker than $\sim$40 nm and could not pick up precipitates smaller than 3 nm, nor any untransformed precipitates. Conventional diffraction contrast microscopy also misses untransformed precipitates, and cannot alone distinguish between precipitates of different types. EELS mapping was the only technique capable both of identifying and measuring Cu-rich precipitates down to 2 nm in diameter with good statistics.

Compared with 3DAP, all of the TEM techniques have better statistics for visible precipitates but are less reliable for detecting smaller precipitates. All of the TEM techniques allow the characterization of large areas containing many precipitates with minimum effort in sample preparation. The two mapping techniques both allow Cu-rich precipitates to be identified. EDX mapping is a relatively straight forward technique to use and does not require much post-acquisition data processing. The drawback is that, with the microscope used, small precipitates are not imaged. EELS mapping has been shown here to be the only technique capable of analysing both small and big precipitates. The disadvantages are the tedious post-acquisition data processing, the need of a clean sample to avoid contamination, and the requirement for a stable stage without much spatial drift.

5. Conclusions

A combination of 3DAP, EDX and EELS mapping and HREM allows a complete characterization of Cu-rich precipitates in ferritic steels. EELS mapping alone in a microscope which provides a spatial resolution of 1 nm or better for energy losses of the order of the Fe L_{23} edge allows a satisfactory analysis of all but the smallest precipitates.

Acknowledgments

We thank the EPSRC, Rolls Royce and the Institute of Nuclear Safety System (INSS), Japan, for support for this work. JMT was further supported by the Royal Academy of Engineering, BNFL and INSS.

References

1. A. V. BARASHEV, S. I. GOLUBOV, D. J. BACON, P. E. J. FLEWITT and T. A. LEWIS, *Acta Mater.* **52** (2004) 877.
2. G. E. LUCAS, G. R. ODETTE, R. MAITI and J. W., SHECKHERD, 13th International Symposium on Influence of Radiation on Materials Properties, 1987, p. 379.
3. P. J. OTHEN, M. L. JENKINS, G. D. W. SMITH and W. J. PHYTHIAN, *Phil. Mag. Lett.* **64** (1991) 383.
4. P. J. OTHEN, M. L. JENKINS and G. D. W. SMITH, *Phil. Mag.* A **70** (1994) 1.
5. H. A. H. DUPARC, R. C. DOOLE, M. L. JENKINS and A. BARBU, *Phil. Mag. Lett.* **71** (1995) 325.
6. R. MONZEN, M. IGUCHI and M. L., JENKINS, *ibid.* **80** (2000) 137.
7. S. ISHINO, Y. CHIMI, BAGIYONO, T. TOBITA, N. ISHIKAWA, M. SUZUKI and A. IWASE, *J. Nucl. Mater.* **323** (2003) 354.
8. R. G. CARTER, N. SONEDA, K. DOHI, J. M. HYDE, C. A. ENGLISH and W. L. SERVER, *ibid.* **298** (2001) 211.
9. P. M. RICE, R. E. STOLLER and J. BENTLEY, in Proc. Microscopy and Microanalysis, (Jones and Begell Publishing, Kansas City, Missouri, 1995) p. 542.
10. M. K. MILLER, B. D. WIRTH and G. R. ODETTE, *Mater. Sci. Eng. A-Structural Materials Properties Microstructure and Processing* **353** (2003) 133.

11. Y. NAGAI, K. TAKADATE, Z. TANG, H. OHKUBO, H. SUNAGA, H., TAKIZAWA and M. HASEGAWA, *Phys. Rev.* **B67** (22) (2003) 224202-1-6
12. D. VAUMOUSSE, A. CEREZO and P. J. WARREN, *Ultramicroscopy* **95** (2003) 215.
13. S. LOZANO-PEREZ, J. M. TITCHMARSH and M. L. JENKINS, EMAG 2003, (Oxford, Institute of Physics Publishing, 2003), p. 241.
14. A. CEREZO, T. J. GODFREY, S. J., SIJBRANDIJ, G. D. W. SMITH and P. J. WARREN, *Rev. Sci. Instrum.* **69** (1998) 49.
15. S. J. SIJBRANDIJ, A. CEREZO, T. J. GODFREY and G. D. W. SMITH, *Appl. Surf. Sci.* **94–5** (1996) 428.
16. P. J. OTHEN, *Thesis, University of Oxford,* 1992.
17. S. LOZANO-PEREZ, J. M. TITCHMARSH and M. L. JENKINS, *Ultramicroscopy* **106**(2) (2006) 7591.